

Island Wakes in Deep Water

CHANGMING DONG, JAMES C. MCWILLIAMS, AND ALEXANDER F. SHCHEPETKIN

Institute of Geophysics and Planetary Physics, University of California, Los Angeles, Los Angeles, California

(Manuscript received 21 October 2005, in final form 12 September 2006)

ABSTRACT

Density stratification and planetary rotation distinguish three-dimensional island wakes significantly from a classical fluid dynamical flow around an obstacle. A numerical model is used to study the formation and evolution of flow around an idealized island in deep water (i.e., with vertical island sides and surface-intensified stratification and upstream flow), focusing on wake instability, coherent vortex formation, and mesoscale and submesoscale eddy activity. In a baseline experiment with strong vorticity generation at the island, three types of instability are evident: centrifugal, barotropic, and baroclinic. Sensitivities are shown to three nondimensional parameters: the Reynolds number (Re), Rossby number (Ro), and Burger number (Bu). The dependence on Re is similar to the classical wake in its transition to turbulence, but in contrast the island wake contains coherent eddies no matter how large the Re value. When Re is large enough, the shear layer at the island is so narrow that the vertical component of vorticity is larger than the Coriolis frequency in the near wake, leading to centrifugal instability on the anticyclonic side. As Bu decreases the eddy size shrinks from the island breadth to the baroclinic deformation radius, and the eddy generation process shifts from barotropic to baroclinic instability. For small Ro values, the wake dynamics is symmetric with respect to cyclonic and anticyclonic eddies. At intermediate Ro and Bu values, the anticyclonic eddies are increasingly more robust than cyclonic ones as Ro/Bu increases, but for large Re and Ro values, centrifugal instability weakens the anticyclonic eddies while cyclonic eddies remain coherent.

1. Introduction

a. Background

Much research has been done to understand the physical processes in the wakes of islands and headlands (e.g., Barkley 1972; Pattiaratchi et al. 1987; Wolanski and Hamner 1988; Aristegui et al. 1994; Heywood et al. 1996; Dietrich et al. 1996; Barton et al. 2000; Aiken et al. 2002; Coutis and Middleton 2002; Harlan et al. 2002; Neill and Elliott 2004; Doglioli et al. 2004; Caldeira et al. 2005). Enhancement in productivity and biomass around islands and the general biological impact of wakes have received much attention (e.g., Hamner and Hauri 1981; Hernandez-Leon 1991; Dower et al. 1992; Martinez and Maamaatuaiahutapu 2004; Hasegawa et al. 2004). Environmental effects have also been studied since the water is partially trapped and particulates accumulate around islands (Rissik et al. 1997).

The study of the wake behind an obstacle has a long history in fluid dynamics (e.g., Batchelor 1967). In the classical problem with horizontal flow and uniform density in a nonrotating frame, a flow passing an obstacle is well characterized by the Reynolds number (Gerrard 1978),

$$Re = \frac{UD}{\nu}, \quad (1)$$

where U is the unperturbed upstream velocity, D is the horizontal scale of the obstacle, and ν is the molecular kinematic viscosity. A series of photographs of the flow regimes obtained at different Re values is presented in Van Dyke (1982). If $Re < 1$, flow separation does not occur, and the flow is symmetric upstream and downstream. If $1 < Re < 40$, a laminar separation is obtained with two steady vortices downstream from the obstacle. At moderate Reynolds numbers, $40 < Re < 10^3$, the steady vortices are replaced by a periodic “von Kármán vortex street,” and finally, for $Re > 10^3$, the separated flow becomes increasingly turbulent and temporally irregular.

In the presence of stable density stratification and rotation and with a very large Re value, oceanic and

Corresponding author address: Dr. Changming Dong, IGPP, University of California, Los Angeles, 405 Hilgard Avenue, Los Angeles, CA 90095-1567.
E-mail: cdong@atmos.ucla.edu

atmospheric wakes can differ significantly from homogeneous, nonrotating wakes with relatively low Re values (Boyer and Davies 2000). With large Re the flow is expected a priori to be fully turbulent. The common use of an eddy viscosity, $\nu_e (\gg \nu)$, in a numerical model allows a possible comparison with the classical wake, but it entails the important issue of how to estimate an appropriate value for ν_e . A Reynolds number based on the eddy viscosity,

$$Re_e = \frac{UD}{\nu_e}, \quad (2)$$

is thus an important nondimensional parameter for modeling geophysical wakes.

In a homogeneous, rotating fluid, both the Reynolds number and Rossby number (Ro) determine the eddy shedding. Here Ro is defined by

$$Ro = \frac{U}{fD}, \quad (3)$$

where f is the Coriolis parameter. Laboratory experiments and theoretical and numerical studies show that increasing the rotation rate tends to inhibit the shedding of eddies (e.g., Boyer and Davies 1982; Walker and Stewartson 1972; Page 1985; Heywood et al. 1996). With a differential background rotation frequency (i.e., $\beta \neq 0$), a wake can develop the structure of a standing Rossby wave (McCartney 1975), and the flow separation and eddy formation are affected by the direction of the incident current with respect to the wave propagation (e.g., Merkin 1980; Johnson and Page 1993; Tansley and Marshall 2001). For eastward flow past an island, the β effect inhibits the separation and formation of an attached eddy, while in a westward flow it does not have a significant influence.

For wakes in a stratified flow, the baroclinic Froude number,

$$Fr = \frac{U}{NH}, \quad (4)$$

represents the ratio of inertial and buoyancy forces; H is the vertical scale (e.g., set by the upstream flow and density stratification profiles) and N is a characteristic magnitude for the Brunt–Väisälä frequency,

$$N = \sqrt{-\frac{g}{\rho_0} \frac{\partial \rho}{\partial z}} \quad (5)$$

(g is the gravitational acceleration, ρ is the upstream density profile, ρ_0 is a mean density, and z is the upward vertical coordinate). Lin and Pao (1979) reviewed stratified, nonrotating wakes with the distinctive behaviors of wake collapse (i.e., a reduction of the vertical extent of the wake behind the obstacle), internal wave

radiation, and downstream emergence of vertically thin (pancake) vortices when $Fr < 1$.

When both rotation and stratification are dynamically influential, the scenario differs from that above. For a flow past a submerged solid obstacle with moderate values of Re , laboratory experiments by Boyer and Chen (1987) indicate that increasing density stratification (decreasing Fr) suppresses vertical motion, inhibits flow over the obstacle, and causes recurrent vortex shedding to occur behind the obstacle at smaller values of Re than in more weakly stratified flows. Their data indicate that the Strouhal number,

$$St = \frac{D}{TU}, \quad (6)$$

associated with recurrent eddy shedding at a time interval T is not affected significantly by changes in the Burger number,

$$Bu = \left(\frac{Ro}{Fr}\right)^2 = \left(\frac{R_d}{D}\right)^2, \quad (7)$$

where R_d is the baroclinic deformation radius,

$$R_d = \frac{NH}{f}. \quad (8)$$

An oceanographically important distinction is between shallow and deep water wakes, depending upon whether the dominant boundary stress is associated with the nearshore bottom or the lateral side of the island (Tomczak 1988). In the shallow-water case, bottom drag is the primary source of vorticity generation (Wolanski et al. 1984, 1996; Pingree and Maddock 1979; Signell 1989; Signell and Geyer 1991; Furukawa and Wolanski 1998; Alaei et al. 2004; Neill and Elliott 2004). Furthermore, lateral vorticity generated by bottom stress can be tilted into vertical vorticity of significance in the wake flow (Smolarkiewicz and Rotunno 1989). In the contrasting deep-water case, the influence of bottom drag and vortex tilting are not important. This latter circumstance can be obtained in a model (e.g., in this paper) by the combination of vertical island sides and a surface-intensified upstream flow. Using a rotating, reduced-gravity model, Heywood et al. (1996) shows eddy shedding that is inhibited by an increase in the rotation rate (i.e., decrease in Ro). Coutis and Middleton (2002) numerically investigate a three-dimensional wake around an isolated island. With a realistic island geometry and a strong incident current (0.7 m s^{-1} at the surface and decaying linearly to zero within a 3-km water column), vortex shedding occurs in the wake. When the incoming flow decreases by half (halving the Ro value), the wake turns into a pair of counterrotating vortices. In their experiments, the Re_e value had to be kept below $500 \text{ m}^2 \text{ s}^{-1}$ to avoid computational

instability. Their analysis focuses on observational comparisons and interpretation of the biological signals in the wake.

b. The present study

The cited literature on oceanic wake investigations, though somewhat fragmentary, shows that there are significant differences between stratified, rotating wakes and homogeneous, nonrotating ones. To more systematically understand these differences, this paper investigates the rotating, stratified deep water wake for three-dimensional flow around a cylindrical island with a horizontally uniform, surface-intensified incident flow. The effects of a topographic profile on the flanks of the island are thus excluded here (pending a systematic study in future). The assumption of $\beta = 0$ is made for simplicity (i.e., the results are relevant for small islands with $\beta D/f \gg 1$). The targeted parameter regime has large Re_e , modest Ro , and intermediate Bu values, and their sensitivities are explored.

The paper is organized as follows: in section 2 the numerical model and configuration are introduced; in section 3 the baseline experiment and modeling results are analyzed in detail; in section 4 the wake sensitivities to Re_e , Bu , Ro , and model resolution are discussed; and section 5 is the summary and discussion.

2. Computational model

a. Model configuration

The Regional Oceanic Modeling System (ROMS) solves the rotating primitive equations. It is a split-explicit, free-surface oceanic model, where short time steps are used to advance the surface elevation and barotropic momentum equations with a larger time step used for temperature, salinity, and baroclinic momentum (Shchepetkin and McWilliams 2005). A third-order, upstream-biased advection operator allows the generation of steep gradients in the solution, enhancing the effective resolution of the solution for a given grid size when the explicit viscosity is small (Shchepetkin and McWilliams 1998). The numerical diffusion implicit in the upstream-biased operator allows the explicit viscosity to be set to be zero without excessive computational noise or instability. However, to examine how Re_e effects the wake formation and evolution, different horizontal eddy viscosity values ν_e are used (section 4a).

For the deep-water island wake problem, the oceanic depth H_m is assumed to be uniform and, for simplicity, the island shape is idealized as a cylinder of diameter D centered at (x_0, y_0) . The model domain is rectangular with incoming flow from the western boundary. At the upstream boundary the incoming flow and density are

prescribed in both the meridional and vertical directions. The zonal current only has vertical shear,

$$u(z) = u_{m1} - u_{m2} \tanh\left(\frac{z + h_s}{h_d}\right), \quad -H_m < z < 0, \quad (9)$$

where $u_{m1} + u_{m2}$ and $u_{m1} - u_{m2}$ are near-surface and bottom currents, respectively; h_s and h_d are the central depth and thickness of the shear layer. The incoming meridional and vertical currents are set to zero.

The upstream density profile is determined from (9) by thermal wind balance,

$$\rho(y, z) = \rho_0 + \frac{\rho_0}{g} \int_{y_0}^y f \frac{\partial u}{\partial z} dy + \delta\rho \tanh\left(\frac{z + h_c}{h_t}\right), \quad (10)$$

where $\delta\rho$, h_c , and h_t are thermocline parameters for one-half of the density difference, central depth, and thickness, respectively. The parameters are constrained so that $\rho(y, z)$ is gravitationally stable [i.e., $\partial\rho(y, z)/\partial z \leq 0$ everywhere within the domain]. The upstream surface elevation is determined from (9) by geostrophic balance,

$$\eta(y) = -\frac{f(y - y_0)}{g} u|_{z=0}. \quad (11)$$

Equations (10) and (11) imply that isopycnal surfaces slope upward to the north and the sea level decreases northward, respectively.

At the northern and southern sides, slippery-tangential and zero-normal boundary conditions are applied. At the eastern outflow boundary, a clamped condition for the outgoing current and the density profile with a sponge layer is used. The solid boundary around the island has a zero-normal and no-slip flow implemented through a standard land-mask algorithm (Shchepetkin and O'Brien 1996). (The solutions presented here have insignificant internal gravity wave energy or open boundary reflection.) The surface momentum, heat, and freshwater fluxes are set to zero. At the flat bottom a bottom stress is applied that is linearly proportional to the horizontal bottom velocity with a friction coefficient of $2.0 \times 10^{-4} \text{ m s}^{-1}$; for our solutions, with weak bottom velocities due to the upstream velocity profile, this coefficient implies a damping time scale of about one month, and it exerts little influence on the flow evolution. The initial condition for the entire domain is set equal to the upstream boundary condition except at the island points with land masks.

b. Explicit eddy viscosity and dissipative advection schemes

Before presenting the numerical experiments, we discuss why a dissipative advection scheme with zero explicit viscosity can work well in oceanic models.

Viscosity plays a dual role in the Navier–Stokes equation: one role is “internal” viscosity, which is responsible for redistributing vorticity (i.e., basically diffusing, while preserving the number of distinct extrema) and dissipating kinetic energy, and the other role is “boundary” viscosity, which is responsible for enforcing a tangential no-slip boundary condition and thereby sustaining a stress. In laminar flows these two viscosities are equivalent in the sense that they come from the same underlying physical process—molecular kinetic exchange of momentum—and, not surprisingly, they have the same value. This equivalence leads to a well-posed characterization of flow regimes by the Reynolds number. In turbulent flows this equivalence breaks down. From the perspective of the macroscopic fluid dynamics (i.e., averaged over small-scale eddy motions that are themselves only weakly or indirectly controlled by molecular viscosity), the two physical roles are distinct: the internal role is controlled by eddy mixing and turbulent cascade as it occurs in approximately homogeneous turbulence, while the boundary role is controlled by boundary layer turbulence with distinctive similarity scaling (e.g., a very different mixing length scale approaching a solid boundary). As a result, one can no longer introduce a well-defined eddy viscosity that is applicable for both roles.

For oceanic circulation modeling, where almost always some important dynamical processes are only marginally resolved (at best), this justifies the practice of independent parameterizations for internal dissipation and boundary conditions. Extensive modeling experience shows that an eddy viscosity parameterization is excessively damping of turbulent flows at the limited grid resolutions that are practically feasible. One can argue that eddy hyperviscosity—either as an explicit biharmonic operator or as an implicit effect built into a truncation term of the advection operator, in our case the third-order upstream scheme—constitutes a minimally sufficient parameterization capable of “absorbing” the turbulent cascade by removing enstrophy from the smallest scales, while introducing only a mild damping effect on the resolved turbulent flow. With an explicit hyperviscous operator, the hyperviscosity value is chosen experimentally to optimize these effects. With implicit advection schemes, the magnitude of the diffusive effect depends on the grid size and adapts to the local flow partem, and a typical solution is marginally rough on the grid scale and thus has some appearance of noisiness, albeit to a controlled degree.

Mathematically speaking, hyperviscosity introduces a higher-order differential operator that requires an additional set of boundary conditions. However, because there is no reasonable expectation that this parameter-

ization is capable of adequately describing boundary layer processes, the choice of additional boundary conditions needed by the operator can be resolved merely for numerical convenience and, as a practical matter, the solutions are not sensitive to details of this choice.

Conversely, tangential no-slip boundary conditions are mathematically needed for Navier–Stokes equations only if the viscosity is finite, while advection does not need any further boundary condition beyond non-normal flow. In a numerical model the discretization of the advection operator involves spatial interpolations that do require an artificial set of boundary conditions in the vicinity of solid boundaries. These extra conditions do not have a prototype in the continuous equations and are based on physical considerations that mimic a no-slip rule. They are implemented by an appropriate land-masking rule (section 2a). As the result, the numerical model “feels” a no-slip boundary even when the explicit eddy viscosity is set to zero because it is always implied that there is an underlying boundary layer with a no-slip condition at the wall.

Physical correctness is a nontrivial issue for oceanic models that are based on physically rationalized but nonfundamental parameterizations for unresolved fluid dynamics. Ultimately this issue can only be addressed by judging the consequences. The substitution of a physical boundary layer with a numerical one can be justified by the integral properties of its effect, such as the total amount of circulation (i.e., integrated vorticity) generated at either side of the island (section 3c). In our scheme the maximum tangential velocity near the side of the island does not change significantly with resolution. Neither does the vorticity integrated over the width of the boundary layer, even though the thickness of the boundary layer itself and the magnitude of the vorticity are both numerically controlled by the grid scale and thus discretely approximate a vortex sheet (section 4a). Once the boundary-generated vortex sheet detaches from the boundary, an accurate numerical representation of the subsequent evolution is controlled by the ability of the code to simulate advective transport and vortex roll-up while smoothing and dissipating underresolved features.

3 Baseline experiment

a. Physical configuration

In the baseline experiment, the domain size is 180 km in the zonal and 80 km in the meridional directions. The center of an island is located one-fourth of the domain away from the upstream boundary and in the middle of the y range (i.e., $x_0 = 45$ km, $y_0 = 40$ km). The island diameter is $D = 20$ km, and the water depth is $H_m =$

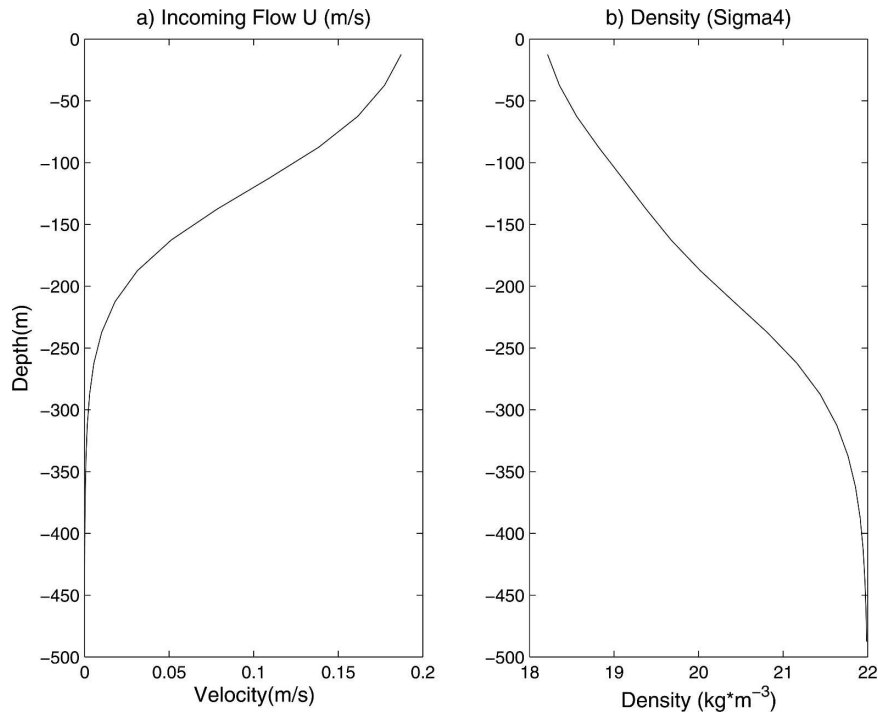


FIG. 1. Vertical profiles of incoming downstream (left) flow and (right) density at $y=y_0$.

500 m (well below the incoming shear and stratification layers). The Coriolis frequency f is set to a constant value of 10^{-4} s^{-1} . The explicit eddy viscosity ν_e is set to zero. In this case, Re takes to infinity, however the effective Re remains finite when the upstream-biased advection operator is applied. In section 4a, one can see that the numerical solutions are insensitive to Re when it becomes large.

With the parameter choices $u_{m1} = 0.1 \text{ m s}^{-1}$, $u_{m2} = 0.1 \text{ m s}^{-1}$, $h_s = 120 \text{ m}$, $\delta\rho = 2 \text{ kg m}^{-3}$, $h_c = 200 \text{ m}$, $h_t = 100 \text{ m}$, and $h_d = 80 \text{ m}$, the upstream profiles are plotted in Fig. 1. The current reaches its maximum about 0.2 m s^{-1} at the surface and zero at the bottom. The Ro value is 0.1, implying a relatively strong geostrophic constraint on the flow evolution (at least away from the island boundary). The buoyancy frequency N is about two orders larger than f , and the baroclinic deformation radius R_d is about 20 km; hence $\text{Bu} \approx 1$. Last, the Richardson number, the ratio of the buoyancy frequency and vertical gradient of the current,

$$\text{Ri} = \frac{N^2}{|\partial\mathbf{u}/\partial z|^2}, \quad (12)$$

is significantly bigger than 0.25 in the whole domain. The smallest value in the upstream region is 3.7; this guarantees that no Kelvin–Helmholtz instability is initiated there. Since $\text{Ri} \sim \text{Fr}^{-2}$ in the thermocline, the

Fr value is small enough that no significant internal gravity waves are generated in the wake (cf. Perret et al. 2006).

The horizontal grid spacing is uniform throughout the domain. In the baseline case, $\delta x = \delta y = 250 \text{ m}$. The vertical grid is also uniformly spaced with 20 levels in the vertical direction between $-H_m$ and the surface; that is, $\delta z = 25 \text{ m}$. The baseline grid size is $720 \times 360 \times 20$. The model is integrated for 50 days, which allows about 10 eddy-shedding cycles to occur.

b. Wake instability and coherent vortex emergence

Starting from the initial condition of nearly uniform flow, the wake quickly develops on an advective time scale, $D/2U = 0.5 \times 10^5 \text{ s} \approx 1 \text{ day}$. The streamlines on the northern and southern sides of the island are squeezed apart, and the flows locally accelerate. With the current speed increasing north and south of the island, the pressure decreases toward the lee side of the island and forces a return flow there. The combination of the return and main flows forms two opposite recirculation cells behind the island during an early stage. [A similar process occurs in a homogeneous flow around a cylinder in a nonrotating frame (Zdravkovich 1997).] About a day after initialization, an anticyclonic eddy north of the island detaches from the island and propagates downstream. When the shed anticyclonic

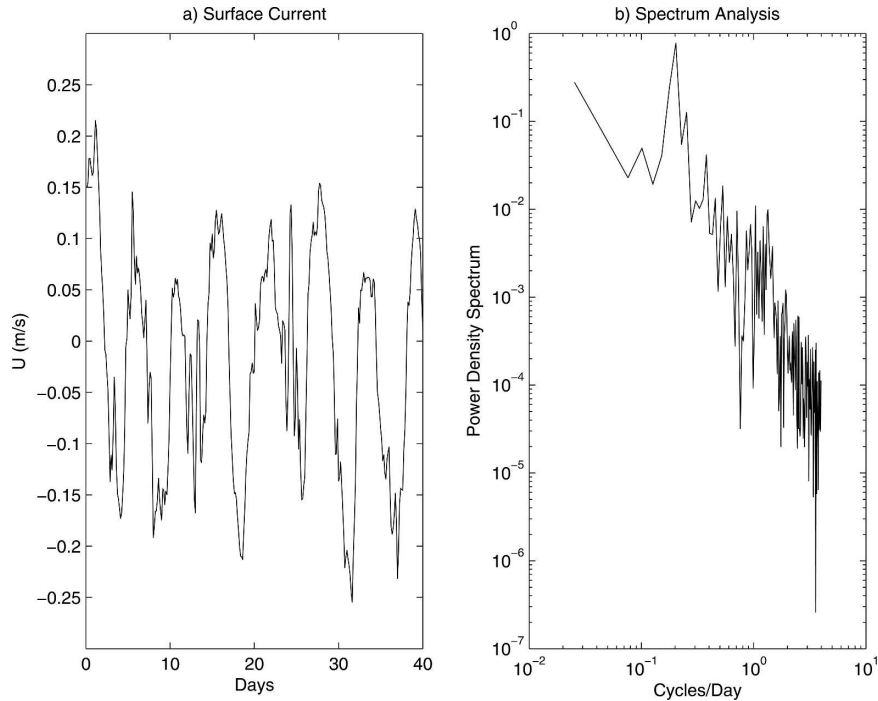


FIG. 2. (a) Time series and (b) frequency spectrum for meridional current at the position 20 km downstream from the center of the island. The peak period is about 5.0 days.

eddy moves downstream, a cyclonic eddy in the south grows larger and separates from the island. After the first pair of eddies detaches from the island, a new pair of eddies form and again detach, etc. The wake appears to be fully developed by about day 4. The eddy-shedding process is quasiperiodic, as seen in Fig. 2a, with a time series of the v velocity at a location 10 km (i.e., D) downstream from the rear edge of the island and along the flow axis. The associated frequency spectrum (Fig. 2b) shows a dominant period of about 5 days. The same dominant period is found at other locations. This period corresponds to a Strouhal number St of 0.23. For experiments in a homogeneous, nonrotating flow, the St value is 0.2 (Zdravkovich 1997). This implies that eddies are shed at a slightly higher frequency in the present configuration.

In this paper, we focus on the fully developed island wake. Two eddy-shedding cycles are shown in Fig. 3. These plots depict the primary elements in the eddy life cycles. Two vortex sheets form and advectively detach from the northern and southern sides of the island. On the southern edge it evolves first into a smooth, wavy pattern and then into a chain of cyclonic eddies that may further merge into larger eddies if they come close enough together farther downstream. On the northern side, the picture is very different: the anticyclonic vortex sheet broadens and fragments into many small ex-

trema whose magnitudes are reduced within the detaching sheet (N.B., the details of this fragmentation are partly obscured by numerical noise since it occurs on a horizontal scale very near the grid resolution). At some distance behind the island, the anticyclonic vorticity ceases to decrease and coalesces into several rather diffuse vortices. The asymmetry between cyclonic and anticyclonic eddies is due to a specific instability happening to anticyclones; in section 3d it is shown to be centrifugal instability. Once the wake eddies are well formed, mutual advection among them governs their motion, along with downstream advection by the mean wake flow. For example, when a weaker eddy approaches a stronger eddy, it rotates around the latter in the direction of its swirling flow.

Figure 4 shows the relative vorticity at four depths levels. Owing to the shape of the incoming velocity (Fig. 1), the wake flow is quite weak at depth. At 200-m depth the wake can be seen only within a downstream distance of about two island diameters and at 300-m depth it has no coherent pattern. The depth structure of eddies is asymmetric between cyclones and anticyclones. This is further illustrated with a vertical section 20 km away from the island center (Fig. 5). In the vorticity field the cyclonic eddy has its maximum at the surface (as does the upstream flow) and is largely confined to within the upper 150 m. In contrast, the anti-

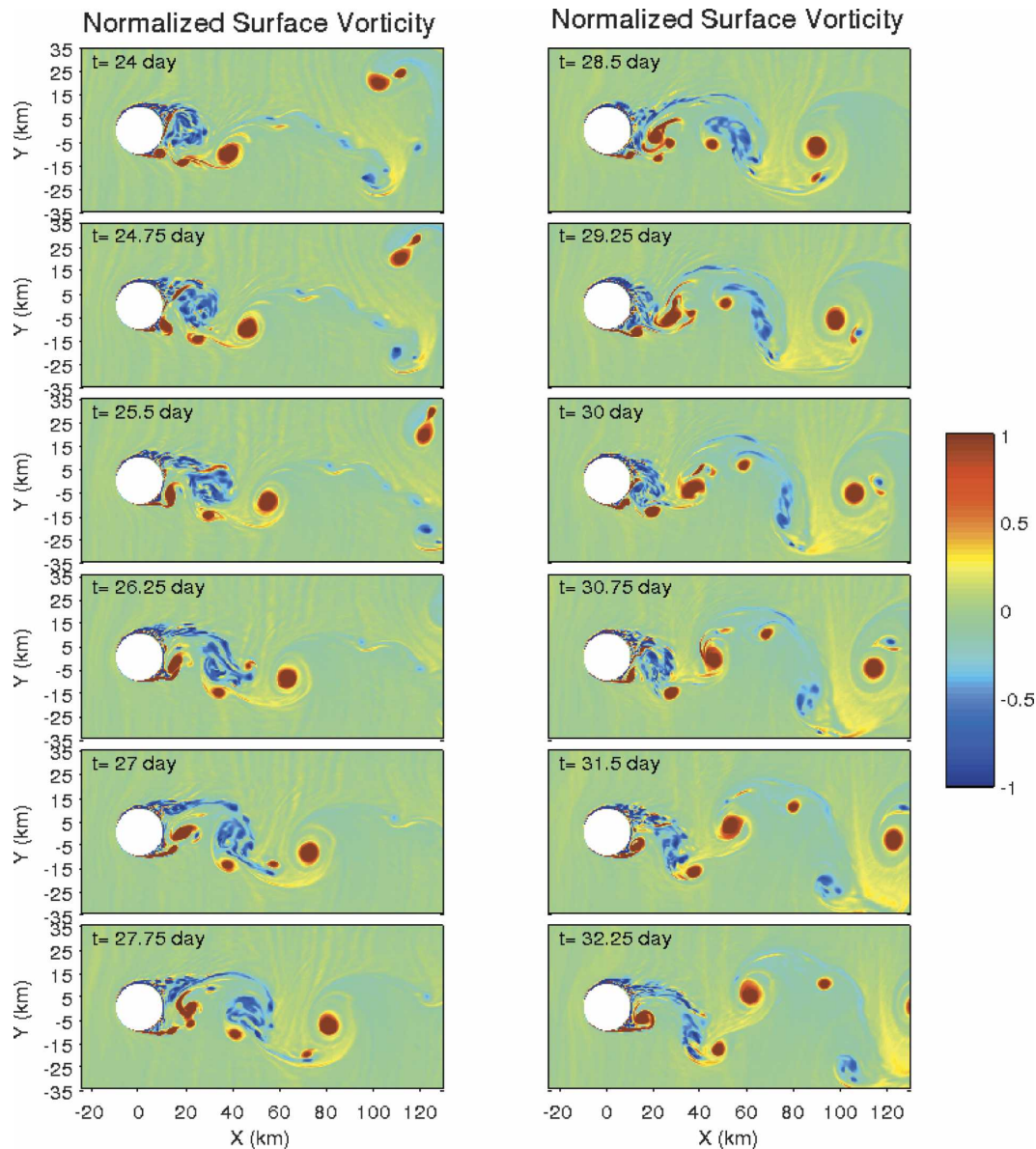


FIG. 3. Sequential maps of surface vertical vorticity (normalized by f) starting from day 24 (i.e., within the quasi-equilibrium period). The time interval is 0.75 days and the duration is 9 days, about two shedding cycles.

cyclonic vorticity has a subsurface maximum around a depth of 130 m and reaches somewhat deeper.

The time-averaged zonal current distribution in the section (the upper-left panel in Fig. 5) shows that the wake is deflected southward by about 5 km relative to the island's lee center, and the peak of the returning flow in the wake is located at the depth of 100 m, the top of the stratification. The horizontal Reynolds stress ($\overline{u'v'}$), which represents the mean momentum flux by fluctuations, is modestly asymmetric between the northern and southern sides of the wake (the upper-right panel in Fig. 5); the asymmetry may be due to

centrifugal instability [section 3d(1)]. The asymmetry between the cyclonic and anticyclonic sides of the wake is also reflected in the density anomaly (the lower-right panel in Fig. 5), defined as the departure from the upstream profile (section 3a). The density increases (decreases) on the northern (southern) side of the island. This reflects geostrophic balance with an enhanced eastward flow downstream of the island edges, relative to the upstream profile, and a diminished eastward flow (even reversed) behind the island. A similar double anomaly structure has been observed in the wake of the Gran Canary Islands (Aristegui et al. 1994). Here the

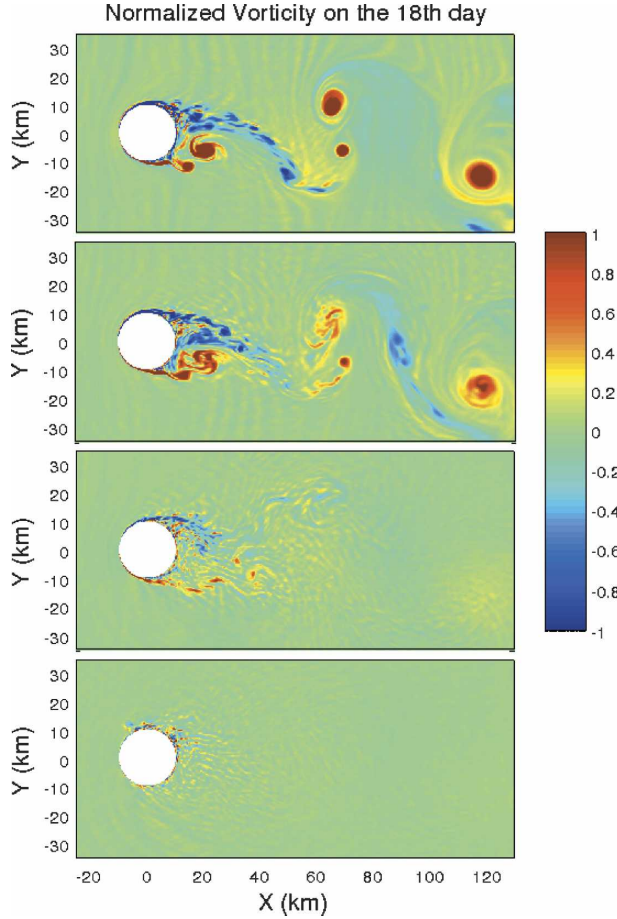


FIG. 4. Normalized vorticity at four depths on day 18: (a) 10, (b) 100, (c) 200, and (d) 300 m.

different-signed anomalies are somewhat different in structure: the cyclonic anomaly has larger Reynolds stress and greater surface intensification than the anticyclonic anomaly.

The asymmetry in the wake also contributes to the generation of a horizontal force on the island in a direction perpendicular to the incident flow, that is, a lift force F_l , which is calculated by

$$F_l = \left(\int_S - \int_N \right) \left(\int_{-H_m}^{\eta} \int_z \frac{\rho g}{\rho_0} dz dz \right) dl, \quad (13)$$

where \int_S and \int_N denote the integration around the southern and northern halves of the island boundary, respectively. After being normalized by the Bernoulli head at the upstream, $(U^2/2)DH_m$, the lift force oscillates around the mean value +0.28 with the amplitude 0.26 and the same frequency as the eddy-shedding frequency. The positive mean lift force (pointing northward) is caused by the asymmetrical wake and resulting asymmetrical pressure distribution around the island

(Chabert D'Hieres et al. 1989). The drag force on the island (the force direction is parallel to the incident flow) can also be estimated by

$$F_d = \left(\int_W - \int_E \right) \left(\int_{-H_m}^{\eta} \int_z \frac{\rho g}{\rho_0} dz dz \right) dl, \quad (14)$$

where \int_W and \int_E denote the integration around the western and eastern halves of the island boundary. The mean drag force normalized by the same quantity is +0.32, pointing downstream.

c. Island vorticity generation

To measure the vorticity generation processes associated with flow adjacent to the island, we analyze an approximate vertical vorticity equation with uniform but anisotropic eddy viscosities, ν_{eh} horizontally and ν_{ev} vertically,

$$\frac{\partial \zeta}{\partial t} + \nabla_h [\mathbf{u}_h (f + \zeta)] \approx \nu_{eh} \nabla_h^2 \zeta + \nu_{ev} \frac{\partial^2 \zeta}{\partial z^2}, \quad (15)$$

where the subscripts h and v denote horizontal and vertical components, respectively. In this approximation, advective terms involving the vertical velocity are neglected since they would enter at $O(\text{Ro}^2)$, relative to the Coriolis term, for small Ro [N.B., due to approximate horizontal nondivergence of \mathbf{u}_h , the leading-order nontrivial balance in (15) actually occurs at $O(\text{Ro})$]. In particular, the so-called tilting term is neglected (cf. Smolarkiewicz and Rotunno 1989).

By volume integrating (15) over an analysis domain containing the island edge, we obtain the following circulation balance:

$$\begin{aligned} \frac{\partial}{\partial t} \left(\iiint \zeta dx dy dz \right) + \int \left[\oint u_n (f + \zeta) dl \right] dz \\ = \nu_{eh} \int \oint (\nabla_n \zeta) dl dz, \end{aligned} \quad (16)$$

where u_n is the normal horizontal velocity along the boundary, ∇_n is the normal gradient, and \oint denotes a line integral integration along the boundary. For a deep water wake with no top or bottom stress, the vertical viscosity term vanishes.

The boundary integrals include both open and solid (island) segments. Because the $u_n = 0$ at the solid boundary, the only advective flux on the left side of (16) comes from the open segment. The eddy viscous flux contribution on the right side can be split into two terms: one along the open boundary and the other

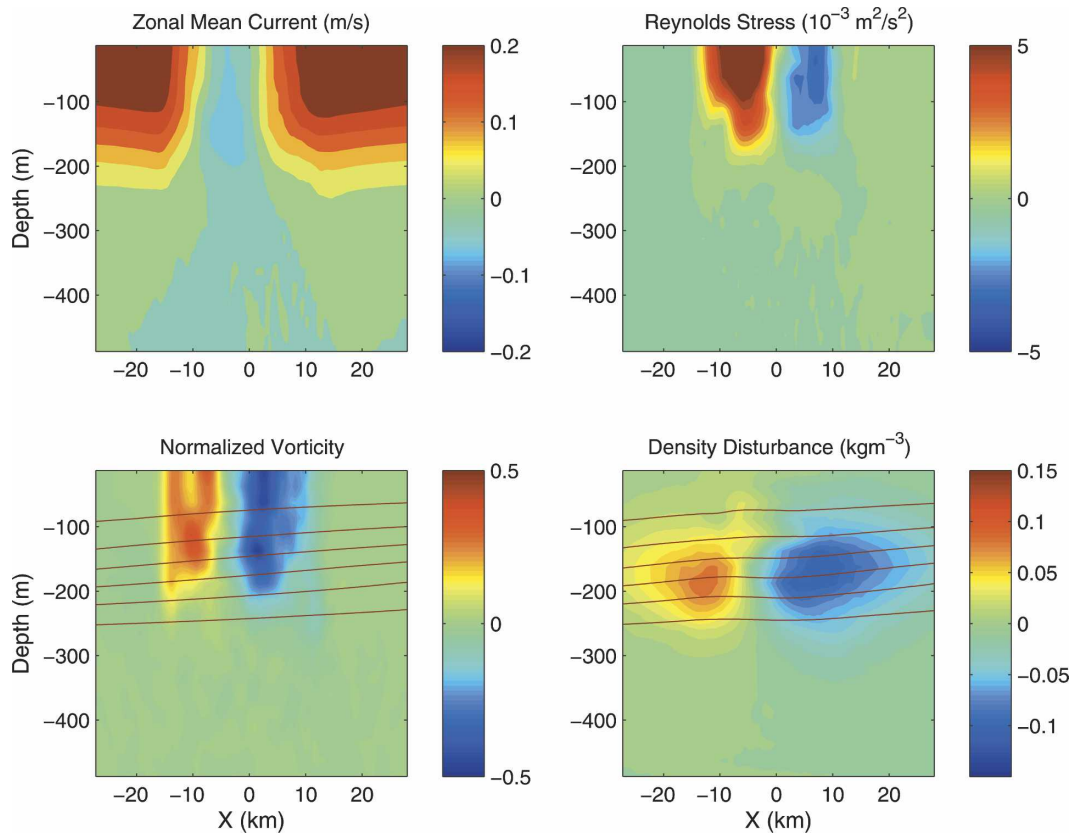


FIG. 5. Time-averaged quantities (over 9 days) in a (y, z) section located 20 km downstream from the island center: (top left) zonal current, (top right) horizontal Reynolds stress, (bottom left) vorticity normalized by f , and (bottom right) density anomaly relative to the upstream field. Contours in the bottom panels are for total density.

along the island. The second term is actually the vorticity generation rate at the island, denoted as V_G . It is not directly calculable by our computational procedure

(section 2), but it can be evaluated diagnostically as a residual from the circulation balance. Therefore, we rewrite (16) as

$$V_G = \underbrace{\frac{\partial}{\partial t} \left(\iiint \zeta \, dx \, dy \, dz \right)}_{\text{tendency } (V_T)} + \underbrace{\iint \left[\oint_{\mathcal{O}} u_n (f + \zeta) \, dl \right] dz}_{\text{advective flux } (V_P)} - \underbrace{v_{eh} \iint \left[\oint_{\mathcal{O}} (\nabla_n \zeta) \, dl \right] dz}_{\text{eddy-viscous flux } (V_D)}. \quad (17)$$

The right-side terms are, respectively, the circulation tendency and the advective and eddy viscous fluxes of ζ across the open boundaries. The symbol $\oint_{\mathcal{O}}$ denotes the line integral along the open boundary segment.

Since cyclonic vorticity is generated along the southern edge of the island and anticyclonic along the northern edge, we separate the model domain into northern and southern halves to distinguish these two opposite-signed source regions. Furthermore, we restrict the combined integration domain for (16) and (17) to a $60 \text{ km} \times 60 \text{ km}$ square centered on the island (i.e., with $60 \text{ km} \times 30 \text{ km}$ halves); this avoids any contributions from

the model's exterior boundary conditions. Figure 6 shows 9-day time series of the terms in (17) for the southern and northern half domains. Although instantaneous fluctuations of the circulation tendency and open boundary flux can be large, in association with eddies passing out of the analysis subdomain, the island vorticity generation rate V_G is relatively steady in time. Furthermore, it is nearly symmetric between cyclonic and anticyclonic generation, with time-averaged values of 6.12 ± 1.81 and $-6.40 \pm 1.65 \text{ m}^3 \text{ s}^{-2}$ in the southern and northern half domains, respectively. This implies that the strong asymmetries seen in the downstream

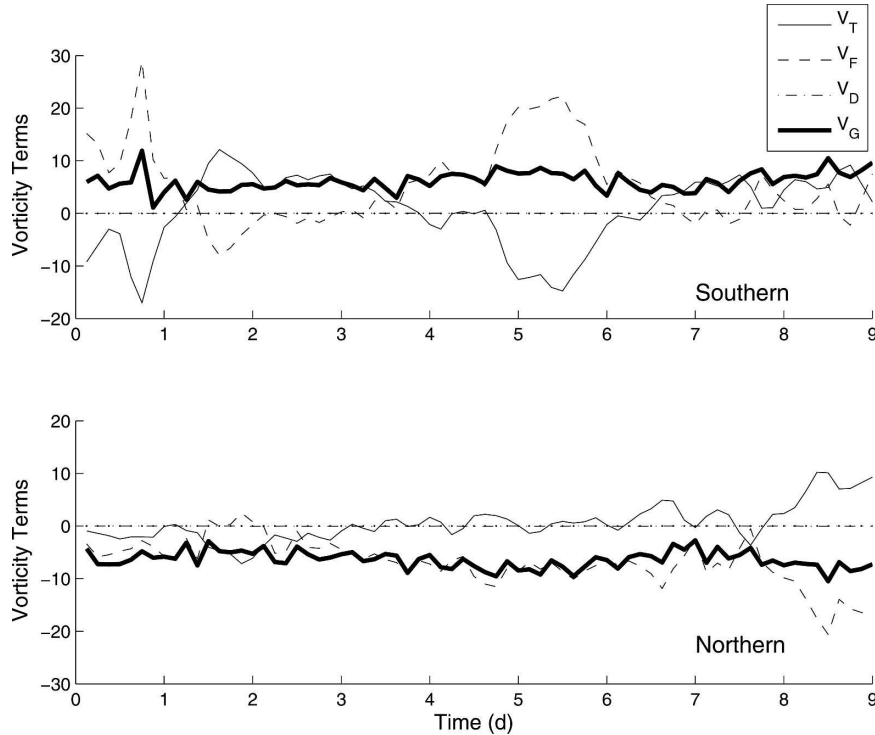


FIG. 6. Island vorticity generation: the volume-integrated vorticity (i.e., circulation) generation rate in the (top) southern and (bottom) northern half domains. See text for term definitions. The time-averaged vorticity generation is $6.12 \pm 1.81 \text{ m}^3 \text{ s}^{-2}$ ($-6.40 \pm 1.65 \text{ m}^3 \text{ s}^{-2}$) in the southern (northern) domains.

wake are manifestations of the evolutionary development in the free stream after separation from the island boundary layers (sections 3b and 4c). We varied the size of the analysis domain to test whether the eddy generation diagnosis is sensitive to this choice; the resulting time series for V_G is nearly the same (not shown), so this method of its determination is robust. Its dependence on Re_e , hence on the mixture of implicit and explicit diffusion in the model, is assessed in section 4a.

d. Wake instability

In the baseline experiment, three types of fluid instability occur in the island wake. First, as in a classical wake, the large horizontal shear within the lateral boundary layer at the island induces a lateral shear instability. Second, the evolutionary asymmetry in the cyclonic and anticyclonic eddies, described above, is due to centrifugal instability. Third, the stratification in a rotating frame allows a conversion of available potential energy by baroclinic instability, especially when the island size D is as large or larger than the deformation radius R_d .

1) CENTRIFUGAL INSTABILITY

The condition for centrifugal instability, at least for inviscid, symmetric flows, is the occurrence of a sign change in Ertel potential vorticity or absolute circulation within the flow (Ooyama 1966; Hoskins 1974; Shen and Thomas 1998). In stable stratification this may be approximated more simply as a change in sign of the absolute vorticity,

$$A = f + \zeta = f \left(1 + \frac{\zeta}{f} \right). \quad (18)$$

This condition will be satisfied near an anticyclonic vorticity minimum that is more negative than $-f$; thus, for an island wake it may occur in the boundary layer on the northern side of the island and downstream after separation. Alternatively, in terms of a local Rossby number defined as $|\zeta|/f$ [cf. the bulk Ro in (3)], centrifugal instability occurs in anticyclonic regions where it is larger than one.

To confirm the occurrence of the centrifugal instability in the baseline experiment, we track one cyclonic eddy and one anticyclonic eddy along their paths in the wake. Figure 7 shows a time series of $\max(\zeta/f)$ within

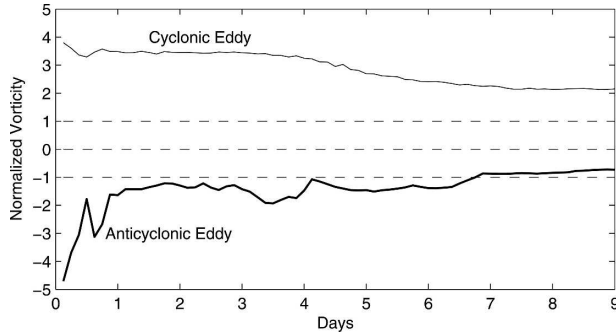


FIG. 7. Normalized peak vorticity within individual cyclonic and anticyclonic eddies as each propagates downstream in the island wake. The dashed lines indicate vorticity values of f , 0, and $-f$, respectively.

these eddies. Starting from approximately equal initial vorticity magnitudes, both anticyclonic and cyclonic extrema decrease with time as the eddies move downstream, partly due to eddy viscous diffusion. However, the anticyclonic vorticity decreases much faster than cyclonic vorticity on an approximately advective time scale, $D/2U = 0.5 \times 10^5$ s, until it is only slightly more negative than $-f$. In contrast, the cyclonic vorticity magnitude stays above $2f$ for about 10 days. We interpret the rapid weakening of the anticyclonic eddy as a manifestation of centrifugal instability.

2) BAROTROPIC AND BAROCLINIC INSTABILITY

Energy budgets can be used in quantifying the relative importance of instability and eddy-mean interaction mechanisms. When the volume-integrated conversion of mean kinetic energy to eddy kinetic energy, $\{K_m K_e\}$, is positive, it implicates barotropic instability, and when volume-integrated conversion of eddy potential energy to eddy kinetic energy, $\{P_e K_e\}$, is positive, it implicates baroclinic instability (Harrison and Robinson 1978). We refer to these two quantities as barotropic and baroclinic conversion, respectively. Volume-integrated energy budget equations can be derived for mean and eddy kinetic energy (K_m and K_e) and mean and eddy available potential energy (P_m and P_e). The barotropic and baroclinic conversions relevant to eddy kinetic energy can be expressed in the following:

$$\{K_m K_e\} = - \left(\overline{u'u'} \frac{\partial \bar{u}}{\partial x} + \overline{u'v'} \frac{\partial \bar{u}}{\partial y} + \overline{u'w'} \frac{\partial \bar{u}}{\partial z} + \overline{v'u'} \frac{\partial \bar{v}}{\partial x} + \overline{v'v'} \frac{\partial \bar{v}}{\partial y} + \overline{v'w'} \frac{\partial \bar{v}}{\partial z} \right) \quad \text{and} \quad (19)$$

$$\{P_e K_e\} = - \frac{g}{\rho_0} \overline{\rho'w'}. \quad (20)$$

Figure 8 shows the horizontal distribution of the vertically integrated energy conversion. On the upper panel of Fig. 8 is $\{K_m K_e\}$. The active barotropic conversion is within the distance of two diameters of the island and is largest at about one diameter away from the island. Near the island there are strips of $\{K_m K_e\} > 0$ north and south of the island where vorticity generation is large. Conversion of the opposite sign takes place immediately behind the island. Integrated over the whole domain, positive conversion is obtained, which implies the importance of barotropic instability in the island wake. Interestingly, the cyclonic and anticyclonic regions do not show a great asymmetry in $\{K_m K_e\}$ despite the dynamical asymmetry of their product vortices (Fig. 7).

On the lower panel of Fig. 8 is the baroclinic energy conversion term $\{P_e K_e\}$. Immediately behind the island is an area where the baroclinic conversion is positive in the same location where the barotropic conversion is negative. Several diameters behind the island there is also a region of weak positive baroclinic conversion. However, on the southern side of the wake is the largest negative region for $\{P_e K_e\}$; it is collocated with the pathway where the dominant cyclonic vortices emerge (Figs. 3–4) and the wake's density anomaly is largest (Fig. 5, left); that is, it is where kinetic energy in the separated flow is converted into potential energy in strong cyclones. Nevertheless, $\{P_e K_e\}$ is generally smaller than $\{K_m K_e\}$, indicating that barotropic conversion is the dominant mechanism for eddy generation in this baseline experiment with $Bu \approx 1$ (but also see section 4a). Integrated horizontally over the whole domain, the baroclinic conversion is negative.

4. Parameter sensitivities

In this section we examine how the wake behavior in the baseline experiment (section 3) changes with eddy viscosity, stratification, rotation rate (i.e., with Re_e , Bu , and Ro), and grid resolution.

a. Reynolds number

In a homogeneous, nonrotating flow past an obstacle, the Reynolds number (Re) is the important control parameter (section 1). It still has an important influence on rotating, stratified wakes, at least up through the transitions with increasing Re that lead to the baseline experiment (section 3). In our model the relevant Re is defined in (2) as Re_e , based on the explicit eddy viscosity ν_e . However, because of the implicit diffusion in the upstream-biased advection operator (section 2), Re_e

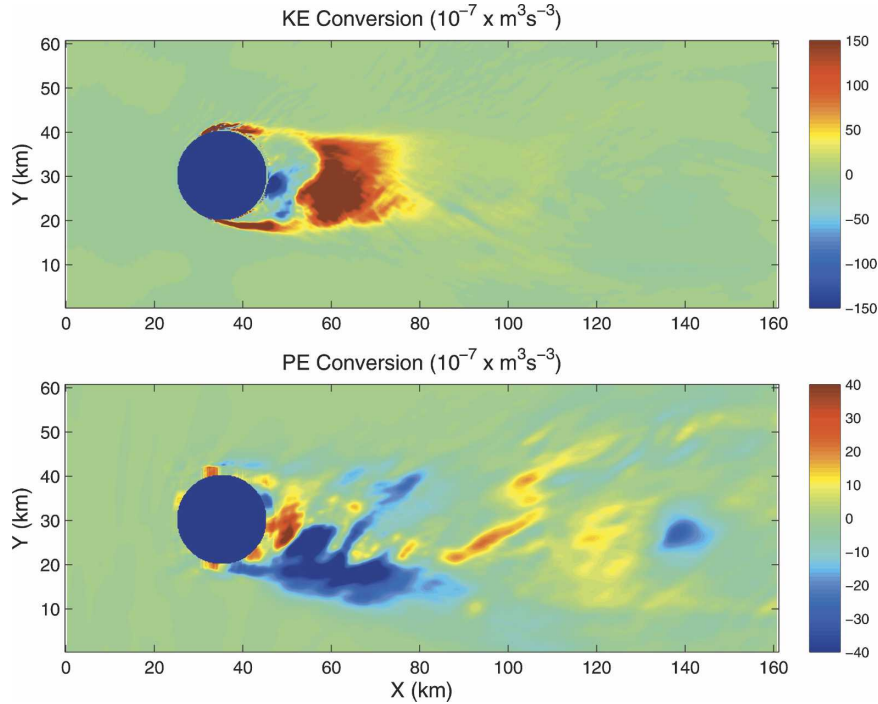


FIG. 8. Depth-integrated, time-averaged energy conversion density: (top) $\{K_m K_e\}$ between mean and eddy kinetic energies and (bottom) $\{P_e K_e\}$ between eddy potential and eddy kinetic energy. Note the scale change between the panels.

can be taken to infinity while the effective Re remains finite.

Figure 9 shows the surface vorticity on around day 20 for different Re_e values varying from 20 to infinity (i.e., only with implicit viscosity). When $Re_e = 20$, two symmetric, steady eddies occur on the lee side of the island. As Re_e increases the eddies develop transient meanders in the wake, and at $Re_e \approx 100$ the vortices detach from the island. The separation threshold is higher than the $Re = 40$ value in a nonrotating, homogeneous flow (Zdravkovich 1997), as expected (section 1). A fine-scale vorticity pattern occurs near the island between the rear stagnation and separation points; we interpret it as computational noise induced by the land mask (section 2), but it does not seem to contaminate the physically meaningful behavior. A small vorticity sheet with opposite sign is caused by a return current flowing opposite to the main current in the immediate lee side of the island. With further increases in Re_e beyond 1600, the eddy shedding and evolution become less dependent on Re_e and converge to a certain pattern; for the case shown, anticyclonic eddies become unstable and weaken while cyclonic eddies are stronger and more coherent.

The Re_e directly affects the boundary shear around the island that is the vorticity source (section 3c). The

upper panel of Fig. 10 plots the horizontal current profiles at $x = x_0$ for a sequence of Re_e values. The horizontal shear increases with Re_e , at least up to a limit set by the grid spacing and the implicit diffusion of the advection operator. We define a measure of the boundary layer thickness as the distance of the current maximum from the island; the lower panel of Fig. 10 shows that, when Re_e is small, the boundary layer thickness increases with decreasing Re_e , but, when Re_e is large, the thickness is less affected by Re_e . If we fit the boundary layer thickness dependence to a power law $\sim Re_e^{-\alpha}$, then α is between $1/4$ and $1/2$ for small Re_e [cf. $\alpha = 1/4$ derived by Walker and Stewartson (1972) for a homogeneous, rotating, viscous lateral boundary layer].

Figure 11 shows how the vorticity generation rate varies with Re_e . For small Re_e , V_G increases with Re_e , while for larger Re_e (beyond the onset of wake turbulence; cf. Fig. 9), V_G converges to a value independent of the eddy viscosity ν_e . Changes in Re_e increase the vorticity magnitude in the shear layer, as expected from the decreasing boundary layer thickness (Fig. 10). The velocity shear near the island is the source of barotropic instability [section 3d(2)], so increasing shear enhances the wake instability and increases the eddy kinetic energy (Fig. 12, upper panel). It also increases the total enstrophy in the flow (lower panel), defined by

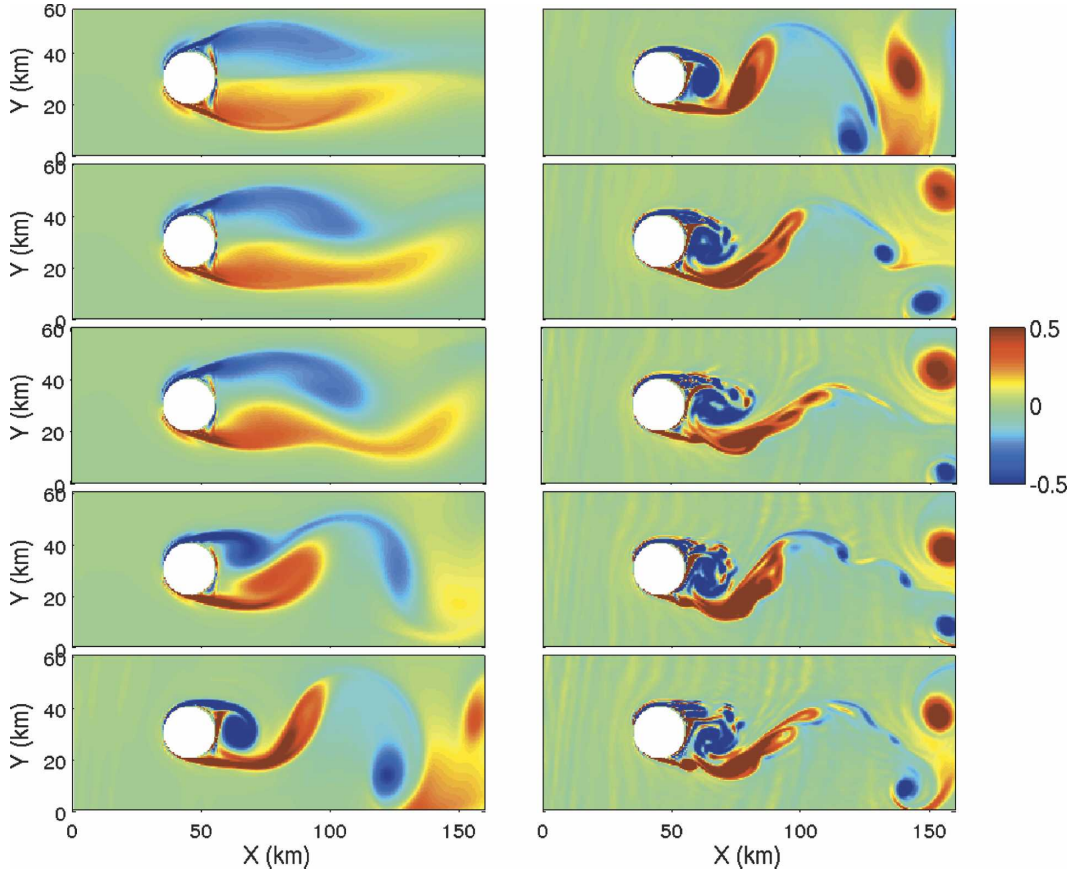


FIG. 9. Normalized surface vorticity patterns for different values of Re_e : (left-hand side, top to bottom) 20, 30, 40, 100, and 400, and the vorticity on day 20 is plotted. (right-hand side, top to bottom) Re_e : 800, 1600, 3200, 6400, and ∞ (i.e., with only with implicit viscosity) with the time of plot adjusted to give a better pattern correspondence among the cases (i.e., at day 19.75, 19.58, 18.13, 17.75, and 17.75, respectively).

$$En = \iiint \xi^2 dx dy dz. \quad (21)$$

For both measures, there is approximate convergence as Re_e becomes large.

Despite increasing shear and eddy strength, the eddy-shedding frequency is almost independent of Re_e : the St value stays almost the same (≈ 0.23) when Re_e ranges from 100 to 6400.

In summary, this analysis shows that the numerical solutions are insensitive to Re when Re becomes large in terms of the following quantities: the surface vorticity, lateral boundary layer, vorticity generation, entrophy, and eddy kinetic energy. In other words, the numerical solutions converge smoothly to the one with zero explicit horizontal eddy viscosity.

b. Horizontal resolution

Since the effective momentum diffusion is controlled by grid resolution when Re_e is small enough (section 2),

we expect some solution variations with δx ($= \delta y$). This is partly because increasing grid resolution in any given situation allows finer structures to emerge in a turbulent flow (e.g., Marchesiello et al. 2003) and partly because the effective Re increases when δx decreases with $\nu_e = 0$ (cf. section 4a).

To examine the effect of horizontal resolution, we made three other experiments using the configuration of the baseline experiment (N.B., with $\delta x = 250$ m) with alternative grid resolutions of 125, 500, and 1000 m, respectively. The total kinetic energy and enstrophy are plotted in Fig. 13. The enstrophy increases strongly with increasing grid resolution, indicating the expected emergence of finer flow structures with smaller δx . Interestingly, the total kinetic energy decreases slightly with increasing grid resolution. The moderate decrease in the total kinetic energy is due to a tendency toward stagnation in part of the wake. The kinetic energy density (not shown) increases near the island, especially on the anticyclonic shear side, but it decreases because of

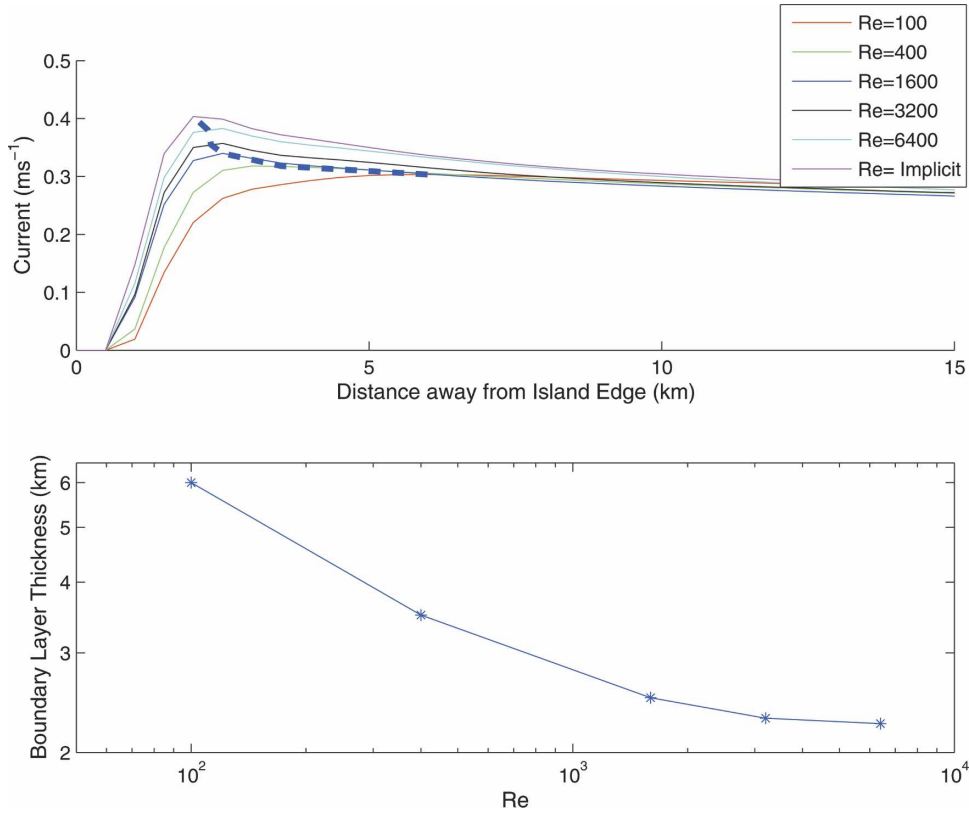


FIG. 10. (top) Cross-stream profiles of downstream velocity adjacent to the island for different values of Re_e . The dashed line indicates the location of the maximum velocity, which is a measure of the boundary layer thickness. (bottom) Boundary layer thickness vs Re_e . When only the implicit viscosity acts (i.e., $\nu_e = 0$, not plotted), the value of the boundary layer thickness is almost equal to that for $Re_e = 6400$.

a wider area and greater degree of stagnation in the far wake, with the latter effect evidently dominating over the former. In Van Dyke (1982) there is a clear tendency increasing Re values for classical wakes to show an expansion of a relatively stagnant area.

c. Burger number

Apart from the boundary layer width, two distinct horizontal scales are found in a rotating, stratified wake: the baroclinic deformation radius (R_d) and the island diameter (D). Their ratio squared is Bu in (7). In the baseline experiment the two scales are approximately equal, and $Bu \approx 1$; the eddy kinetic energy budget [section 3d(2)] has an overall negative contribution from $\{P_e K_e\}$, showing that barotropic conversion is the primary source of eddy energy. We now examine the sensitivity of the baroclinic conversion process to Bu in a sequence of experiments with $\nu_e = 0$.

Figure 14 shows the volume integrated $\{P_e K_e\}$ as a function of $Bu^{-1/2} = D/R_d$, where the Bu value is changed by changing D . When D increases, the volume

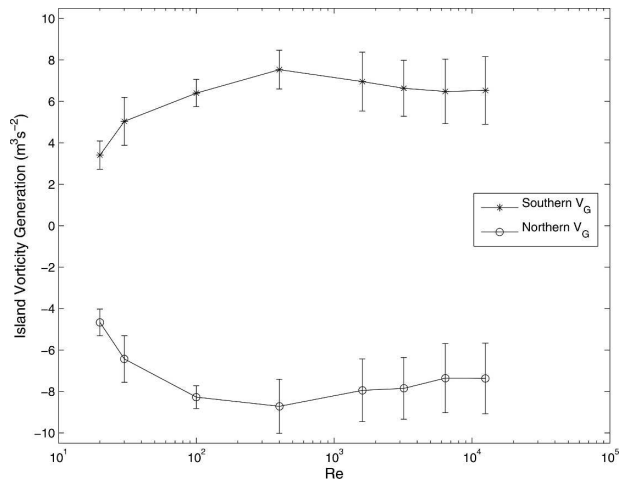


FIG. 11. Time-averaged, volume-integrated vorticity generation rate V_G , as a function of Re_e . The time interval is 9 days. The vertical lines associated with data points are twice the standard deviation of V_G during the period. When only the implicit viscosity acts (i.e., $\nu_e = 0$, not plotted), the V_G value is almost equal to the value for $Re_e = 6400$.

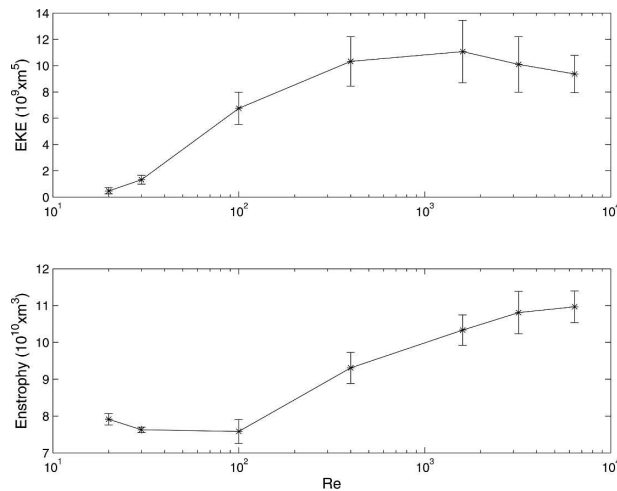


FIG. 12. Variation of volume-integrated (top) eddy kinetic energy and (bottom) enstrophy with Re_e . Experiments are the same as in Fig. 11. When only the implicit viscosity acts (i.e., $\nu_e = 0$, not plotted), the values of both quantities are almost equal to those for $Re_e = 6400$.

integrated $\{P_e K_e\}$ changes sign and becomes positive and large; this indicates that baroclinic instability becomes important. We can refer to a classical baroclinic instability problem to understand this wake dependence on Bu . When the mean current has a uniform vertical shear and is independent of y (i.e., Eady's problem, Pedlosky 1987), the most unstable mode has a disturbance scale somewhat larger than R_d . Viewing the island as a disturbance to the incident flow, baroclinic

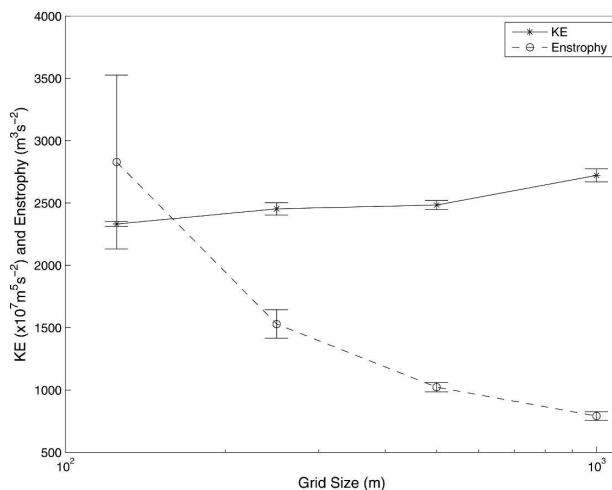


FIG. 13. Sensitivity of time-averaged total kinetic energy and surface enstrophy to changes in the grid resolution δx . The experiments are performed on four grid resolution: 125, 250, 500, and 1000 m. The time averages are calculated over 10 days, and the error bar is equal to the standard deviation with time.

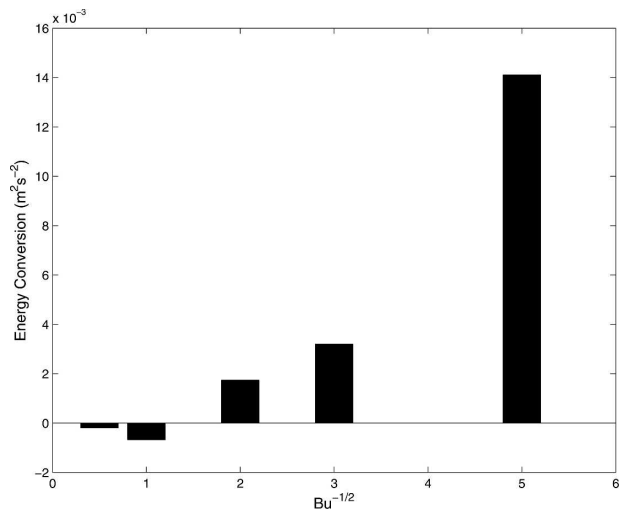


FIG. 14. Time-average, depth-integrated baroclinic energy conversion density $\{P_e K_e\}$, for different values of Bu .

instability is favored when D becomes larger than R_d (i.e., $Bu < 1$).

To see how baroclinic instability affects the vorticity structure, Fig. 15 shows a case when $Bu^{-1/2} = 5$ and strong baroclinic instability occurs. Compared with the baseline experiment, many more eddies are present in the wake, and their mutual interactions are less simply cyclic. When $D \gg R_d$, the dominant eddy size remains somewhat larger than R_d , as expected from baroclinic instability theory. From the time series of the surface vorticity for this case (not shown), we continue to see that anticyclonic eddies are systematically weakened compared to the cyclonic eddies, indicating the continuing occurrence of centrifugal instability even with D is large. When Bu is larger than 1, the eddy size is almost equal to the island size.

d. Rossby number

In the baseline experiment, although the bulk $Ro \approx 0.1$ from (3), a local Rossby number, $|\zeta|/f$, can exceed the threshold criterion for centrifugal instability when ν_e is small enough [section 3d(1)]. This results in the asymmetry between stronger cyclones and weaker anticyclones in the wake (section 3). In this section, we examine the effect of varying Ro .

Figure 16 is a snapshot of the surface vorticity distribution when Ro is made to be as large as 0.5 by decreasing the rotation rate to $f = 0.2 \times 10^{-4} \text{ s}^{-1}$ and keeping $\nu_e = 0$. The mesoscale and submesoscale anticyclonic eddies are almost entirely destroyed by this invigoration of the centrifugal instability process. In contrast, although there is evident fine structure in the instability region near the island, the cyclonic eddy

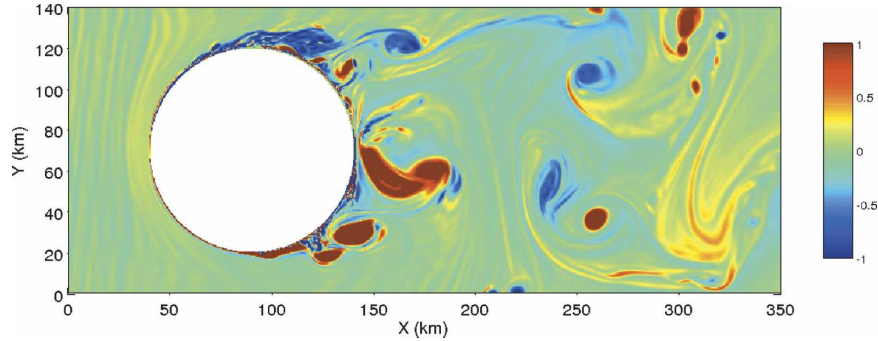


FIG. 15. Normalized surface vorticity snapshot for a wide island with 100-km diameter.

evolves coherently in a way that is broadly similar to the smaller Ro value in Fig. 3. (Some skepticism is warranted for this solution with its very large values of $|\zeta|/f$ calculated with a hydrostatic approximation.)

With laboratory wake experiments for intermediate Bu , moderate Re , and intermediate Ro values, Perret et al. (2006) shows that the anticyclonic wake eddies become more coherent while the cyclonic eddies elongate and weaken when the parameter $\lambda = Ro/Bu = Fr^2/Ro$ increases (λ is a scaling estimate for the nondimensional size of a vertical displacement of an isopycnal surface with the assumptions of geostrophic, hydrostatic balance, and vertical advection of mean stratification as the cause of density fluctuations). There is a substantial antecedent literature also showing anticyclonic vortex dominance at finite Ro and Bu values in computational solutions. The computational literature is reviewed in Graves et al. (2006), and a theoretical explanation is presented for how anticyclonic vortices are less strongly deformed than cyclones during transient straining events and thus lose less energy and potential enstrophy in relaxing back to an equilibrium axisymmetric state. This regime of anticyclonic eddy dominance is opposite to the cyclonic dominance in the baseline experiment (section 3) and it comes entirely from flows that are centrifugally stable (i.e., $|\zeta|/f < 1$).

To explore the regime with smaller values of Ro , both globally and locally, then either the upstream flow must be reduced or the island boundary layer thickness must be kept from becoming too small so that the vorticity it generates is not too large relative to f . For a deep water island this can be accomplished either by reducing the bulk Ro with weaker upstream flow or stronger f , or by decreasing Re_e by increasing ν_e (section 4a). For the latter option, we choose a value of $Re_e = 400$ as small enough to limit the local Rossby number but large enough to be within the regime of a turbulent wake, and perform a sequence of experiments additionally varying Bu . Figure 17 shows how the normalized vorticity difference between cyclonic and anticyclonic eddies downstream of the island varies with $\lambda = Ro/Bu$. The three curves represent experiments with different Re_e : one is for implicit viscosity only and the other two are for the $Re_e = 1600$ and 400. The curves span several different dynamical regimes. For small enough Ro with any Bu value, λ is small, and there is the dynamical symmetry that is expected in the quasigeostrophic limit. As Ro increases or Bu decreases and λ increases toward a value near one, significant vortex asymmetries arise. The sense of the asymmetry, however, differs between the moderate and high Re_e experiments; anticyclones dominate in

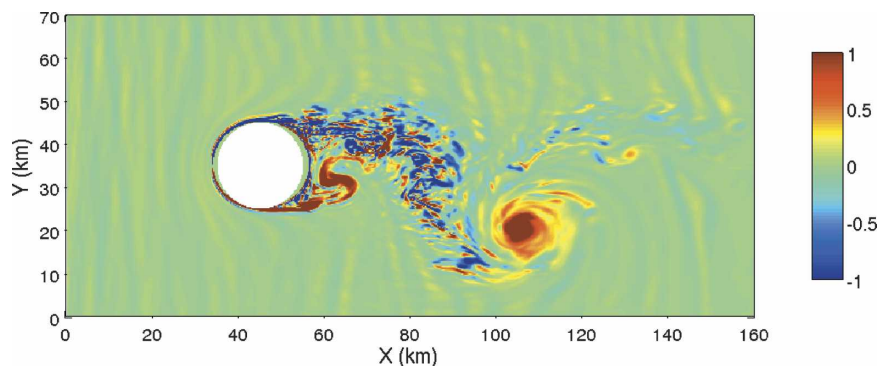


FIG. 16. Normalized surface vorticity snapshot on day 8 with a large Ro value of 0.5.

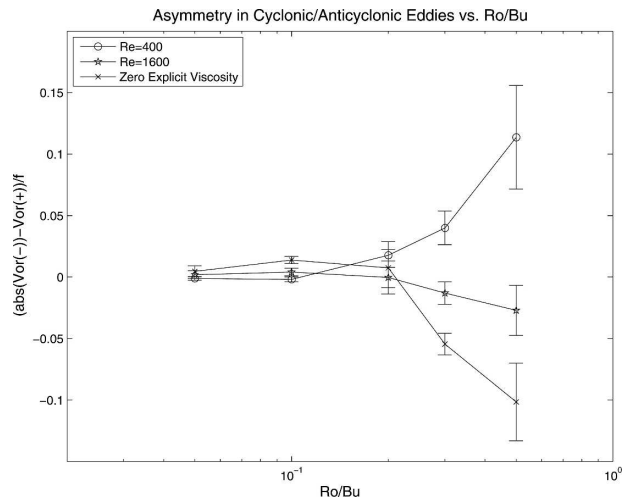


FIG. 17. Asymmetry in anticyclonic and cyclonic eddies as a function of $\lambda = \text{Ro}/\text{Bu}$ for different values of Re_e (inset): the difference between negative and positive vorticity extrema over the entire domain for an eddy-shedding cycle. The error bar is equal to the standard deviation over several eddy cycles.

the former case when centrifugal instability does not occur, and cyclones are dominant in the latter case when it does. These different behaviors are illustrated in Fig. 18.

The velocity frequency spectrum is dominated by the eddy-shedding frequency. The frequency can be characterized by St in (6), and Fig. 19 shows that St increases with λ . When the emergent eddies are smaller than D , they occur more frequently relative to an advective rate set by the island size, U/D . This result is in agreement with laboratory experiments (Perret et al. 2006).

5. Summary and discussion

In this paper we use a high-resolution numerical model to investigate the turbulent, deep-water island wake. We focus on a cylindrical island shape in uniformly deep water with a horizontally uniform, surface-intensified incoming flow in a rotating, stratified environment. Such an idealization can sharpen our attention to the essential physical processes in an island wake, such as vorticity generation, wake instability, coherent eddy emergence, and sensitivity to the principal nondimensional parameters. In a baseline experiment with zero explicit viscosity ($\text{Re} = \infty$ and large effective Re) and island-scale parameter values of $\text{Bu} = 1$ and $\text{Ro} = 0.1$, we see manifestations of barotropic, baroclinic, and centrifugal instabilities all occurring in the wake. The centrifugal instability causes asymmetry in

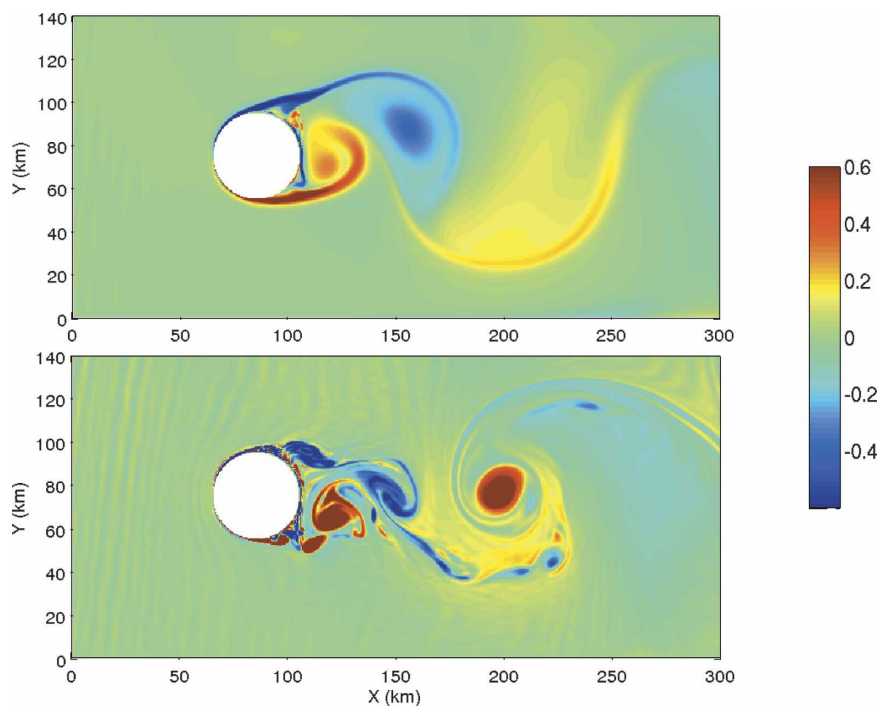


FIG. 18. Examples of asymmetry in anticyclonic and cyclonic eddies: snapshot of the surface vorticity with $\text{Bu} = 0.25$ and different Re_e : (top) $\text{Re}_e = 400$ and (bottom) large Re_e , with only implicit viscosity.

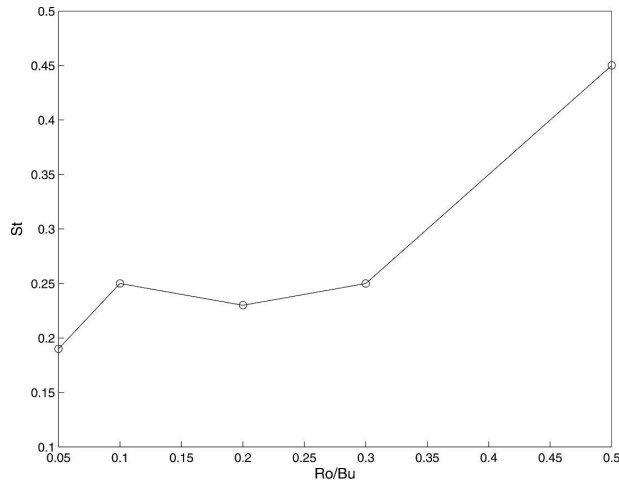


FIG. 19. The dependence of St on $\lambda = Ro/Bu$ for cases with $\nu_e = 0$. The eddy-shedding frequency is determined from the peak in the velocity frequency spectrum that we estimate as typically having a 20%–30% uncertainty based on the sharpness of the peak.

the evolving cyclonic and anticyclonic eddies when the island-generated vorticity exceeds f and the ratio of barotropic to baroclinic energy conversion rates increases with Bu . Through an analysis of the circulation equation, we quantify the rate of vorticity generation by flow past the island. The rotating, stratified wake has a similar behavior to the classic nonrotating, unstratified wake in its sensitivity to Re_e through the regime transitions to flow separation, unsteadiness, and incipient eddy shedding; however, at higher Re_e values, it develops a sequence of nonclassical coherent vortices. With decreasing explicit eddy viscosity ν_e , the solution converges to a highly turbulent state in which the dissipation is controlled by the implicit diffusion in the advection scheme. When the island size D is bigger than the baroclinic deformation radius R_d (i.e., small Bu), the eddy size is controlled by R_d , whereas for large Bu the eddy size is approximately the same as D . The island-scale Ro and Re_e values together control the dynamical asymmetry between cyclonic and anticyclonic eddies. For sufficiently small Ro and Re_e (so that the island boundary layer does not generate vorticity values comparable to f), the dynamics are approximately quasigeostrophic and the two types of eddies behave symmetrically. In contrast, when Ro increases to 0.5 with large Re_e , the mesoscale and submesoscale anticyclonic eddies are almost completely destroyed while the cyclonic eddies stay strong. In the small Ro/Bu regime, the eddies are dynamically symmetric, while in the large Ro/Bu regime, an Re_e -dependent asymmetry occurs: When Re_e is moderate or small, the anticyclonic eddies are dominant over the cyclonic eddies (because

of their greater robustness to perturbations; Graves et al. 2006), but when the Re_e is larger, cyclonic eddies are dominant (because of centrifugal instability of anticyclonic eddies).

Many complex physical processes can occur in an oceanic island wake. For example, the incoming flow can be spatially nonuniform (e.g., an eddy approaching an island; Simmons and Nof 2000) or time varying (e.g., tidal oscillations, where an additional new time scale is introduced; Lloyd et al. 2001; Stansby and Lloyd 2001). When a shelf slope is associated with an island, potential vorticity conservation may restrain the flow from moving too close to the shoreline (Schar and Durran 1997), and bottom drag may be significant (see the references in section 1). Edwards et al. (2004) argue that the wake can also be affected by inviscid lateral stress from bottom pressure, that is, from drag. Smolarkiewicz and Rotunno (1989) propose an inviscid mechanism for vertical vorticity generation when horizontal vorticity is baroclinically generated and then tilted into the vertical direction. Kolyshini and Ghidaoui (2003) analyze the wake instability using the shallow-water equation (with no rotation). The shape of an island can influence the wake structure. The surface wind on the lee side of the island might exhibit sheltering or develop its own wake structures that might influence the oceanic wake (Xie et al. 2001; Caldeira and Marchesiello 2002). Much remains for further investigation.

Acknowledgments. We appreciate support from the National Science Foundation (OCE 06-23011) and the Office of Naval Research (Grants N00014-02-1-0236 and N00014-05-10293). We thank Jeroen Molemaker and Pablo Sangra for fruitful discussions; Yi Chao for his aid in making JPL supercomputers available for this study; and Hongchun Zhang for her help running some of the numerical experiments. The calculations were performed on supercomputers at both JPL and NCSA.

REFERENCES

- Aiken, C., A. Moore, and J. Middleton, 2002: The non-normality of coastal ocean flows around obstacles, and their response to stochastic forcing. *J. Phys. Oceanogr.*, **32**, 2955–2974.
- Alaee, M. J., G. Ivey, and C. Pattiaratchi, 2004: Secondary circulation induced by flow curvature and Coriolis effects around headlands and islands. *Ocean Dyn.*, **54**, 27–38.
- Aristegui, J., P. Sangra, S. Hernandez-Leon, M. Canton, A. Hernandez-Guerra, and J. Kerling, 1994: Island-induced eddies in the Canary Islands. *Deep-Sea Res. I*, **41**, 1509–1525.
- Barkley, R., 1972: Johnston Atoll's wake. *J. Mar. Res.*, **30**, 201–216.
- Barton, E., G. Basterretxea, P. Flament, E. Mitchelson-Jacob, B. Jones, J. Aristegui, and F. Herrera, 2000: Lee region of Gran Canaria. *J. Geophys. Res.*, **105**, 17 173–17 193.

- Batchelor, G. K., 1967: *An Introduction to Fluid Dynamics*. Cambridge University Press, 515 pp.
- Boyer, D. L., and P. Davies, 1982: Flow past a cylinder on a beta plane. *Philos. Trans. Roy. Soc. London*, **306A**, 33–56.
- , and R. Chen, 1987: On the laboratory simulation of topographic effects on large scale atmospheric motion systems: The Rocky Mountains. *J. Atmos. Sci.*, **44**, 100–123.
- , and P. Davies, 2000: Laboratory studies of orographic effects in rotating and stratified flows. *Annu. Rev. Fluid Mech.*, **32**, 165–202.
- Caldeira, R. M. A., and P. Marchesiello, 2002: Ocean response to wind sheltering in the Southern California Bight. *Geophys. Res. Lett.*, **29**, 1635, doi:10.1029/2001GL014563.
- , —, N. P. Nezlin, P. M. DiGiacomo, and J. C. McWilliams, 2005: Island wakes in the Southern California Bight. *J. Geophys. Res.*, **110**, C11012, doi:10.1029/2004JC002675.
- Chabert D'Hieres, G., P. A. Davies, and H. Didelle, 1989: A laboratory study of the lift forces on a moving solid obstacle in a rotating fluid. *Dyn. Atmos. Oceans*, **13**, 47–75.
- Coutis, P., and J. Middleton, 2002: The physical and biological impact of a coastal current on a steep slope in presence of a cape: The case of the Promontorio di Portofino. *J. Geophys. Res.*, **109**, C12033, doi:10.1029/2004JC002422.
- Dower, J., H. Freeland, and K. Juniper, 1992: A strong biological response to oceanic flow past Cobb seamount. *Deep-Sea Res.*, **39A**, 1139–1145.
- Edwards, K. A., P. MacCready, J. N. Moum, G. Pawlak, J. Klymak, and A. Perlin, 2004: Form drag and mixing due to tidal flow past a sharp point. *J. Phys. Oceanogr.*, **34**, 1297–1312.
- Furukawa, K., and E. Wolanski, 1998: Shallow-water frictional effects in island wakes. *Estuarine Coastal Shelf Sci.*, **46**, 599–608.
- Gerrard, T. H., 1978: The wake of a cylindrical bluff bodies at low Reynolds number. *Philos. Trans. Roy. Soc. London*, **288A**, 351–382.
- Graves, P. G., J. C. McWilliams, and M. T. Montgomery, 2006: Vortex evolution due to straining: A mechanism for dominance of strong, interior anticyclones. *Geophys. Astrophys. Fluid Dyn.*, **100**, 151–183.
- Hamner, W. M., and I. R. Hauri, 1981: Effects of island mass: Water flow and plankton pattern around a reef in the Great Barrier Reef lagoon, Australia. *Limnol. Oceanogr.*, **26**, 1084–1102.
- Harlan, J. A., S. E. Swearer, R. R. Leben, and C. A. Fox, 2002: Surface circulation in a Caribbean island wake. *Cont. Shelf Res.*, **22**, 417–434.
- Harrison, D. E., and A. R. Robinson, 1978: Energy analysis of open regions of turbulent flows: Mean eddy energetics of a numerical ocean circulation experiment. *Dyn. Atmos. Oceans*, **2**, 185–211.
- Hasegawa, D., H. Yamazaki, R. G. Lueck, and L. Seuront, 2004: How islands stir and fertilize the upper ocean. *Geophys. Res. Lett.*, **31**, L16303, doi:10.1029/2004GL020143.
- Hernandez-Leon, S., 1991: Accumulation of mesozooplankton in a wake area as a causative mechanism of the “island-mass effect.” *Mar. Biol.*, **109**, 141–147.
- Heywood, K. J., D. P. Stevens, and G. R. Bigg, 1996: Eddy formation behind the tropical island of Aldabra. *Deep-Sea Res. I*, **43**, 555–578.
- Hoskins, B. J., 1974: The role of potential vorticity in symmetric stability and instability. *Quart. J. Roy. Meteor. Soc.*, **100**, 480–482.
- Johnson, E. H., and M. Page, 1993: Flow past a circular cylinder on a β -plane. *J. Fluid Mech.*, **257**, 603–626.
- Kolyshini, A. A., and M. S. Ghidaoui, 2003: Stability analysis of shallow wake flows. *J. Fluid Mech.*, **494**, 355–377.
- Lin, J.-T., and Y.-H. Pao, 1979: Wakes in stratified fluids. *Annu. Rev. Fluid Mech.*, **11**, 317–338.
- Lloyd, P. M., P. Stansby, and D. Chen, 2001: Wake formation around islands in oscillation laminar shallow-water flows. Part 1: Experimental investigation. *J. Fluid Mech.*, **429**, 217–238.
- Marchesiello, P., J. C. McWilliams, and A. F. Shchepetkin, 2003: Equilibrium structure and dynamics of the California Current System. *J. Phys. Oceanogr.*, **33**, 753–783.
- Martinez, E., and K. Maamaatuaiahutapu, 2004: Island mass effect in the Marquesas Islands: Time variation. *Geophys. Res. Lett.*, **31**, L18307, doi:10.1029/2004GL020682.
- McCartney, M., 1975: Inertial Taylor columns on a beta plane. *J. Fluid Mech.*, **68**, 71–95.
- Merkin, L. O., 1980: Flow separation on a beta plane. *J. Fluid Mech.*, **99**, 399–409.
- Neill, S. P., and A. J. Elliott, 2004: Observations and simulations of an unsteady island wake in the Firth of Forth, Scotland. *Ocean Dyn.*, **54**, 324–332.
- Ooyama, K., 1966: On the stability of the baroclinic circular vortex: A sufficient condition for instability. *J. Atmos. Sci.*, **23**, 43–53.
- Page, M. A., 1985: On the low Rossby number of a rotating fluid past a circular cylinder. *J. Fluid Mech.*, **156**, 205–221.
- Pattiaratchi, C., A. James, and M. Collins, 1987: Island wakes and headland eddies: A comparison between remotely sensed data and laboratory experiments. *J. Geophys. Res.*, **92**, 783–794.
- Pedlosky, J., 1987: *Geophysical Fluid Dynamics*. 2d ed. Springer-Verlag, 710 pp.
- Perret, G., A. Stegner, M. Farge, and T. Pichon, 2006: Cyclone–anticyclone asymmetry of large-scale wakes in the laboratory. *Phys. Fluids*, **18**, 036603, doi:10.1063/1.2179387.
- Pingree, R. D., and L. Maddock, 1979: The tidal physics of headland flows and offshore tidal bank formation. *Mar. Geol.*, **32**, 269–289.
- Rissik, D., I. M. Suthers, and C. T. Taggart, 1997: Enhanced particle abundance in the lee of an isolated reef in the south Coral Sea: The role of flow disturbance. *J. Plankton Res.*, **19**, 1347–1368.
- Schar, C., and D. Durran, 1997: Vortex formation and vortex shedding in continuously stratified flows past isolated topography. *J. Atmos. Sci.*, **54**, 534–554.
- Shchepetkin, A. F., and J. J. O'Brien, 1996: A physically consistent formulation of lateral friction in shallow-water equation ocean models. *Mon. Wea. Rev.*, **124**, 1285–1300.
- , and J. C. McWilliams, 1998: Quasi-monotone advection schemes based on explicit locally adaptive dissipation. *Mon. Wea. Rev.*, **126**, 1541–1580.
- , and —, 2005: The Regional Ocean Modeling System: A split-explicit, free-surface, topography-following-coordinate oceanic model. *Ocean Modell.*, **9**, 347–404.
- Shen, C. Y., and T. E. Thomas, 1998: Inertial instability of large

- Rosby number horizontal shear flows in a thin homogeneous layer. *Dyn. Atmos. Oceans*, **26**, 185–208.
- Signell, R. P., 1989: Tidal dynamics and dispersion around coastal headlands. Ph.D. Thesis, Woods Hole Oceanographic Institution, MIT, 162 pp.
- , and W. R. Geyer, 1991: Transient eddy formation around headlands. *J. Geophys. Res.*, **96**, 2561–2575.
- Simmons, H. L., and D. Nof, 2000: Islands as eddy splitters. *J. Mar. Res.*, **58**, 919–956.
- Smolarkiewicz, P. K., and R. Rotunno, 1989: Low Froude number flow past three dimensional obstacles. Part I: Baroclinically generated lee vortices. *J. Atmos. Sci.*, **46**, 1154–1164.
- Stansby, P. K., and P. Lloyd, 2001: Wake formation around islands in oscillation laminar shallow-water flows. Part 2. Three-dimensional boundary-layer modeling. *J. Fluid Mech.*, **429**, 239–254.
- Tansley, C., and D. Marshall, 2001: Flow past a cylinder on a beta-plane with application to Gulf Stream separation and the Antarctic Circumpolar Current. *J. Phys. Oceanogr.*, **31**, 3274–3283.
- Tomczak, M., 1988: Island wakes in deep and shallow water. *J. Geophys. Res.*, **93**, 5153–5154.
- Van Dyke, M., 1982: *An Album of Fluid Motion*. Parabolic Press, 174 pp.
- Walker, J. D. A., and K. Stewartson, 1972: The flow past a cylinder in a rotating frame. *Z. Angew. Math. Phys.*, **23**, 745–752.
- Wolanski, E., and W. M. Hamner, 1988: Topographically controlled fronts in the ocean and their biological influence. *Science*, **241**, 177–181.
- , J. Imberger, and M. L. Heron, 1984: Island wakes in shallow coastal waters. *J. Geophys. Res.*, **89**, 10 553–10 569.
- , T. Asaeda, A. Tanaka, and E. Deleersnijder, 1996: Three-dimensional island wakes in the field, laboratory experiments and numerical models. *Cont. Shelf Res.*, **16**, 1437–1452.
- Xie, S. P., W. T. Liu, Q. Liu, and M. Nonaka, 2001: Far-reaching effects of the Hawaiian Islands on the Pacific ocean–atmosphere system. *Science*, **292**, 2057–2060.
- Zdravkovich, M. M., 1997: *Flow around Circular Cylinders: A Comprehensive Guide through Flow Phenomena, Experiments, Applications, Mathematical Models, and Computer Simulations*. Oxford University Press, 694 pp.